13th International Symposium on Particle Image Velocimetry – ISPIV 2019
Munich, Germany, July 22-24, 2019

PIV experiments to examine the manipulation of large-scale structures using cross-flow jets in a turbulent boundary layer

Z. Ruan[1], C. M. de Silva[2,1*], N. Hutchins[1], I. Marusic[1]

[1] Department of Mechanical Engineering, The University of Melbourne, Melbourne, Australia
[2] School of Mechanical and Manufacturing Engineering, University of New South Wales, Sydney, Australia
[*] c.desilva@unsw.edu.au

Abstract

This study examines the structures in a high Reynolds number turbulent boundary layer that has been perturbed by a spanwise array of cross-flow jets that actively target large-scale motions (LSMs) in the logarithmic region of the flow. To this end, a set of Particle Image Velocimetry (PIV) experiments that employ a multi-camera imaging system are conducted in a turbulent boundary layer at a friction Reynolds number of $Re_\tau \equiv U_\tau \delta/\nu \approx 14{,}000$. In order to capture the large range of spatial scales at high Reynolds numbers, specialist PIV cameras are substituted with modern consumer full-frame digital cameras, which are configured to capture double-exposed images (DE-PIV). Simultaneous skin-friction measurements are also captured upstream of the jet-array in order to actively target the presence of either high-speed or low-speed LSMs. This paper validates the quality of the current DE-PIV measurements against well-resolved hot-wire measurements in an uncontrolled (canonical) turbulent boundary layer at comparable flow conditions. Further, preliminary results are presented through computing phase-averaged flow-fields of the perturbed turbulent boundary layer to examine the modified turbulent structures that have been actively controlled via the wall-normal jets.

1 Introduction

Turbulence skin-friction in turbulent boundary layers, induced by the non-linear interaction of fluid motions at different characteristic length scales, is significant in many engineering applications. In recent decades, studies have revealed the existence of large-scale motions (LSMs) within the logarithmic and outer region of turbulent boundary layers (TBLs) with friction Reynolds Numbers, Re_τ, greater than 2000 (Hutchins and Marusic, 2007). These motions play an important role in the production of turbulent energy and they have been reported to modulate the near-wall turbulence and hence the skin-friction at the surface (Hutchins et al., 2011). Recent experiments conducted by Abbassi et al. (2017) achieved a maximum local skin-friction drag reduction of up to 3.2% through actively weakening the high-velocity LSMs using a spanwise array of wall normal jets. This work builds upon their findings by examining the spatially modified turbulent structures resulting from the identical control scheme using a large field of view (FOV) DE-PIV experiment.

Throughout this work, the coordinate system x, y and z refer to the streamwise, spanwise and wall-normal directions, respectively. Their corresponding instantaneous velocity fluctuations are represented by U, V and W. Overbars denote average quantities and the superscript + refers to normalisation by viscous variables. For example, we use $u^+ = u/U_\tau$ for velocity. Here, $U_\tau \equiv \sqrt{\tau_w/\rho}$ is the friction velocity, where τ_w is the wall shear stress and ρ is the fluid density.

2 Experimental Work

The experiments in this study are conducted in the High Reynolds Number Boundary Layer Wind Tunnel (HRNBLWT) at the University of Melbourne. Figure 1 shows a schematic of the experimental campaign, including details of the real-time control system that selectively targets LSMs and also the PIV

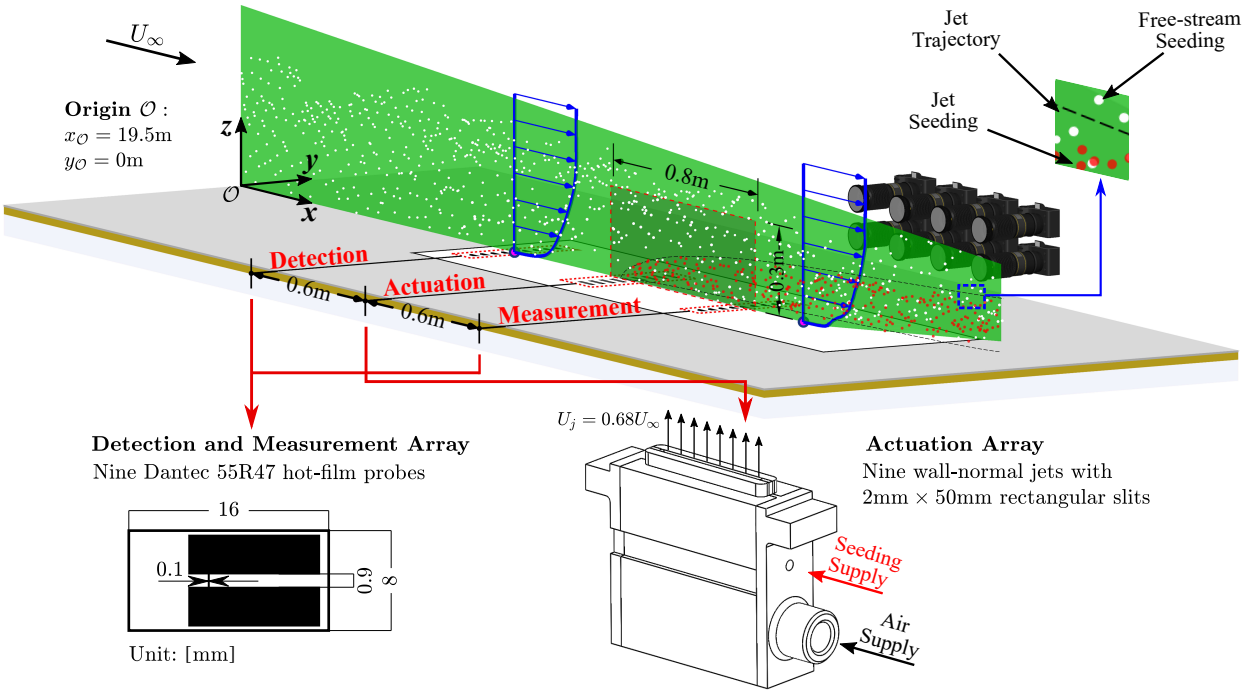

Figure 1: Schematic of the experimental campaign which includes the real-time control system to target the LSMs in the turbulent boundary layer and the components of the PIV system.

system. The PIV imaging system is designed such that we are able to capture spatial flow features over a wide range of scales at a significantly lower cost. With this goal in mind, specialist PIV cameras are substituted with modern consumer full-frame digital cameras, which are typically available at a fraction of the cost. These cameras are configured to capture double-exposed images (DE-PIV), but at a much higher spatial resolution than that available from specialist PIV cameras configured to capture single-exposure images (SE-PIV). Specifically, the imaging system consists of eight 36 megapixel Nikon D810 DSLR cameras, which provide a combined spatial resolution of ≈ 0.3 gigapixels. It should be noted, that the operation of the cameras in DE-PIV mode typically leads to direction ambiguity, however, in turbulent boundary layers flow reversals are rare events, restricted to with the first few wall-units from the wall ($z^+ < 5$) (Lenaers et al., 2012). Therefore the issue of directional ambiguity is not critical in the current study. Further, although the achievable accuracy is less at matched imaging conditions when compared to SE-PIV (de Silva et al., 2018), the higher sensor resolutions afforded from the consumer cameras allows us to use larger interrogation window sizes, without compromising spatial resolution. Laser illumination for the experiments is provided by a 400 mJ/pulse Spectra-Physics PIV-400 Nd:YAG 532nm laser and seeding is injected into the wind tunnel upstream of the flow conditioning, which is then recirculated throughout the whole laboratory (de Silva et al., 2014). Additionally, a second seeding source is employed to independently seed the wall-normal jets.

Because multiple cameras are used here to construct a combined FOV, a calibration procedure is essential to account for distortions within the image plane and also to provide a means to stitch the velocity fields from each camera. Similar to prior multi-camera experiments in the same facility we employ a large calibration target that spans the entire extent of the FOV (de Silva et al., 2012, 2014). The velocity vectors are calculated with LaVision DAVIS 8.4 package using an auto-correlation algorithm with multi-grid (Willert, 1997) and window deformation applied (Scarano, 2001). The databases are processed with 50% overlap and the final interrogation window size for each dataset are detailed in table 1, together with a summary of the flow conditions. Further details on processing the DE-PIV images using a similar experimental configuration can be found in de Silva et al. (2018).

The control architecture of the real-time system includes two spanwise arrays of nine Dantec 55R47 glue-on-type hot-film sensors and a spanwise array of nine wall normal jets with 2 mm × 50 mm (spanwise × streamwise) rectangular slits (see figure 1). The spanwise arrays of sensors and jets employ a spanwise separation of 26 mm ($\approx 0.1\delta$) between each sensor/actuator, covering a total spanwise domain of 210 mm (0.75δ). The array of jets are mounted 0.6 m ($\approx 2.1\delta$) downstream of the upstream detection array. A further measurement array of hotfilm sensors is located 0.6 m ($\approx 2.1\delta$) downstream of the jets (see figure 1). Real-time low-pass filters convolve the friction velocity fluctuations measured by the upstream hot-films (the detection array) to detect the presence of LSMs allowing us to actively actuate the wall-normal jets on

Table 1: Summary of Experimental parameters.

	Smooth Wall	**Opposing control**
Flow Conditions		
U_∞	20.8 m/s	20.2 m/s, ($U_j = 0.68U_\infty$)
Re_τ	≈ 14000	≈ 14000
U_τ	0.67 m/s	0.64 m/s
ν/U_τ	23.4 μm	24.1 μm
Flow medium	Air (atmo.)	Air (atmo.); (Jet 1.8bar)
PIV and Processing Parameters		
Total sensor resolution	$\approx 0.3 \times 10^9$ pixels	
Spatial resolution	≈ 28 μm/pixel (1.1^+)	
Field of view ($x \times y$)	≈ 0.75 m $\times$ 0.25 m ($2.5\delta \times 0.9\delta$)	
$\Delta x \times \Delta y$ (pixels)	96×48 ($105^+ \times 52^+$)	
Laser sheet thickness	≈ 1 mm (40^+)	
Acquisition frequency	1 Hz	2 Hz
Number of images	750	2250

particular flow structures.

To manipulate the LSMs residing in the logarithmic region, the jet velocity is fixed at $U_j = 0.68U_\infty$ to ensure the jets penetrate to the upper bound of the logarithmic region. Three different real-time, control schemes are implemented: **(i) opposing control -** jets fire only at high-momentum events, **(ii) reinforcing control -** jets fire only at low-momentum events, and **(iii) desynchronised control -** jets fire randomly. For each control scheme, the jets are active for the same proportion of the time (each jet has a 50% opportunity to activate during the measurement). In this paper, we present preliminary results from the opposing control scheme and the reference uncontrolled turbulent boundary layer.

3 Results

3.1 Experimental Validation

In order to validate the current PIV configuration, mean-flow and turbulence intensity statistics for the uncontrolled turbulent boundary layer are compared with the existing databases. Specifically, flow statistics from well-resolved hot-wire anemometry measurements by Baidya et al. (2017) and prior PIV measurement by de Silva et al. (2014) from the same facility are compared against the present DE-PIV measurements in figure 2, where (a-c) corresponds to the mean streamwise velocity and the turbulence intensities of the streamwise and wall-normal components, respectively. The results exhibit good agreement between the current PIV experiments (∘ symbols), the hot-wire experiments (−− line) and the PIV experiments of de Silva et al. (2014) (△ symbols). It should be noted, that we expect some degree of spatial attenuation of the smaller energetic scales particularly from the PIV databases, which is a result of the spatial averaging across the interrogation window size and laser sheet thickness (Lee et al., 2016). The magenta solid line corresponds to $\overline{u^2}^+$ computed from the well-resolved hot-wire measurements filtered to the spatial resolution of the present DE-PIV measurement (—). Good agreement is observed confirming that the discrepancy observed in the near-wall region is primarily due to spatial attenuation.

3.2 Instantaneous flow-fields

Figure 3 presents instantaneous snapshots of streamwise (U) and wall-normal (W) velocity contours for the unperturbed canonical boundary layer (a,c) and a boundary layer modified by the opposing control scheme

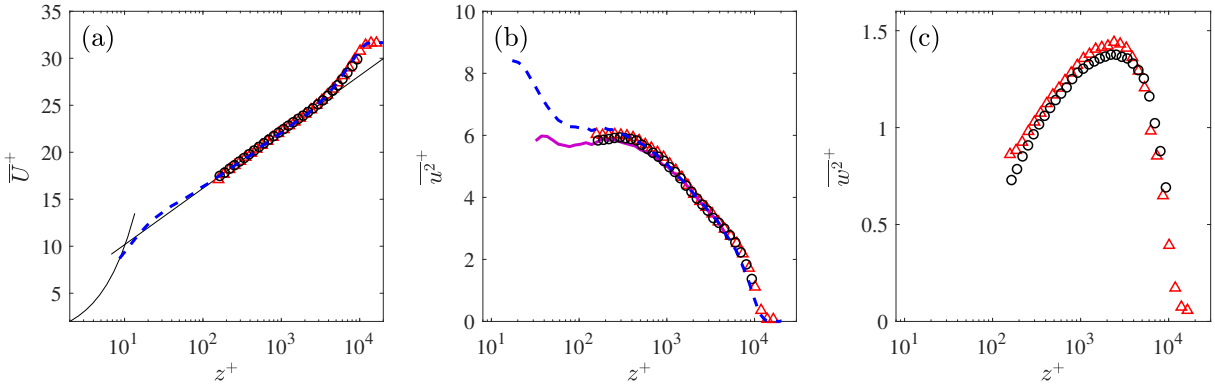

Figure 2: (a, b, c) Mean streamwise velocity, $\overline{U}$ and turbulence intensities, $\overline{u^2}^+$, $\overline{w^2}^+$ for the uncontrolled (canonical) turbulent boundary layer. The ∘ symbols correspond to the present DE-PIV experiments, and the blue dashed-line (−−) and △ symbols correspond to measurements by Baidya et al. (2017) and de Silva et al. (2014), respectively. The magenta solid line (—) corresponds to $\overline{u^2}^+$ from the hotwire measurements filtered to the spatial resolution of the present DE-PIV measurements.

(b,d) where the jet has been active for 46.8 ms. The field-of-view extends ≈ 0.8m in the streamwise direction, which is equivalent to 2.5δ, which provides a uniquely large field-of-view capturing a large extent of the modified LSMs in a high Re turbulent boundary layer. Since the jets are activated based on the presence of LSMs, while the PIV system (laser and cameras) is triggered at a fixed frequency, the TTL trigger signals for both the jets and PIV system are recorded simultaneously using a data-acquisition system. This allows us to precisely temporally situate the PIV images with respect to the duty cycle of the jets during post-processing.

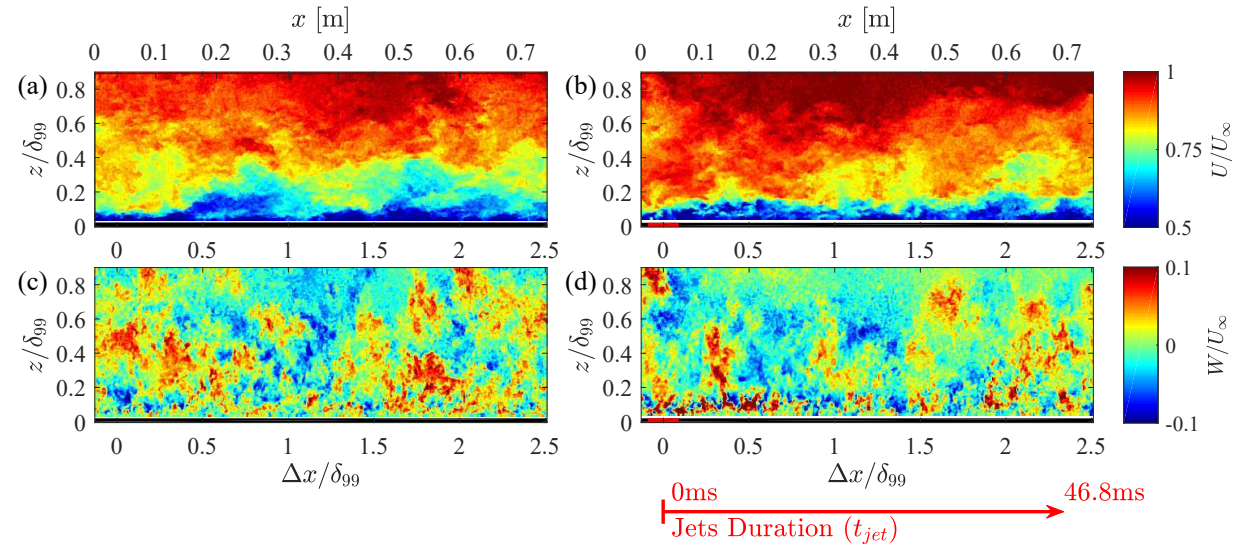

Figure 3: Colour contours of streamwise velocity, U for (a) the uncontrolled scheme (canonical boundary layer) and (c) the opposing controlled scheme. The corresponding instantaneous wall-normal velocity, W, is shown in (b) and (d), respectively. The red arrow indicates the jet firing duration. The red shaded region centred at $\Delta x = 0$ shows the jet location in (b) and (d).

Figure 4 illustrates the opposing control scheme, where the black solid line is the large-scale skin-friction velocity fluctuation, u_{τ_l}, captured from the centre sensor in the upstream detection array of skin friction sensors. These hot-films are calibrated using an *insitu* calibration process, further details on this procedure can be found in Abbassi et al. (2017). For the opposing controlled scheme, the jet fires when u_{τ_l} is positive, i.e when a large-scale high-speed 'footprint' is detected. We define the phase difference between the laser pulse and the preceding jet trigger as the laser delay (τ_h). In a similar fashion, we define the length of the currently actuated structure as, L_s.

To convert the temporal signal from the hot-film sensors into the spatial domain we invoke Taylor's frozen hypothesis, where $\Delta x = -U_c\tau_h$ and U_c corresponds to the mean streamwise velocity at the centre

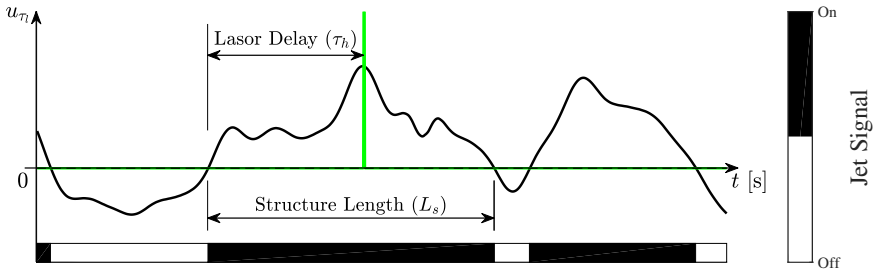

Figure 4: A schematic illustrating the opposing control scheme. τ_h corresponds to the duration between the jet firing and the laser pulse of the PIV system and L_s corresponds to the length of the structure currently being fired on.

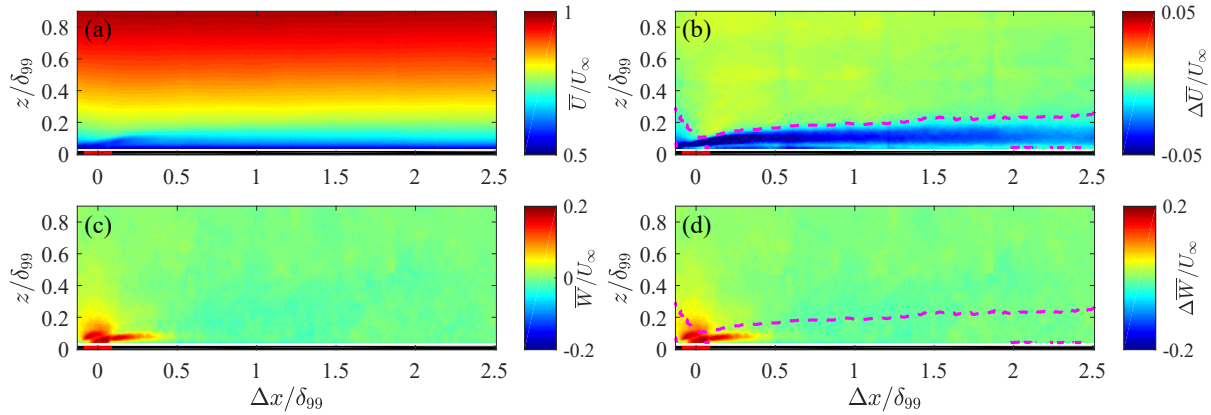

Figure 5: (a, c) contours of the mean streamwise and wall-normal velocity field, $\overline{U}/U_\infty$ and $\overline{W}/U_\infty$ for the opposing controlled boundary layer. (b, d) contours of the difference of $\overline{U}$ and $\overline{W}$ between the uncontrolled reference and opposing control scheme boundary layer, $\Delta\overline{U} = \overline{U}_{op} - \overline{U}_{ref}$ and $\Delta\overline{W} = \overline{W}_{op} - \overline{W}_{ref}$, respectively. The magnate dashed line (−−) shows the contour of $\Delta\overline{U}/U_\infty = -5\times10^{-3}$, which implies the jet trajectory.

of log-region (Hutchins et al., 2011; Mathis et al., 2009). For example, in the snapshots shown in figure 3(b,d), the jet has been activated for 47ms (i.e. $\tau_h = 47$ms). During this time, as indicated by the red arrow, the jet-flow has travelled approximately 2.2δ in the streamwise direction based on Taylor's frozen hypothesis.

3.3 Averaged flow-fields

Figure 5(a,c) presents colour contours of the mean velocity, $\overline{U}$ and $\overline{W}$, across the entire FOV captured with opposing control scheme applied. Owing to the jet flow, a strong positive wall-normal velocity region is present at the jet exit (red rectangle located at $\Delta x/\delta_{99} = 0$) in figure 5. It should be noted that the contours indicate a maximum wall-normal velocity of $\overline{W} \approx 0.2U_\infty$, which is less than the prescribed jet exit velocity $U_j = 0.68U_\infty$ imposed by the jet. However, this behaviour is expected since this is a time-averaged velocity field and the jet does not fire for all images captured. Moreover, we are unable to capture the first 100 viscous units above the wall where we expect the jet signature in W to be strongest.

In order to better visualise the jet trajectory and its influence to the cross-flow, figure 5(b,d) shows the absolute difference of mean streamwise and wall-normal velocity contours between the opposing control scheme and the uncontrolled reference turbulent boundary layers, $\Delta\overline{U} = \overline{U}_{op} - \overline{U}_{sw}$ and $\Delta\overline{W} = \overline{W}_{op} - \overline{W}_{sw}$. The results for ΔU in 5(b) reveals that the jet produces a region of decelerated streamwise velocity that extends well beyond the captured field-of-view of 2.5δ and clearly demonstrates the jet trajectory. Using a contour level of $\Delta\overline{U}/U_\infty = -5\times10^{-3}$, it is evident that the jet flow penetrates to the upper bound of logarithmic region ($z/\delta > 0.15$) (Marusic et al., 2013). In comparison, the influence of the jet flow on the mean wall-normal velocity is constrained to a smaller region immediately downstream of the jet ($\Delta x < 0.5\delta$).

To further elucidate the influence of the jet-flow the turbulent energy is investigated in Figure 6,

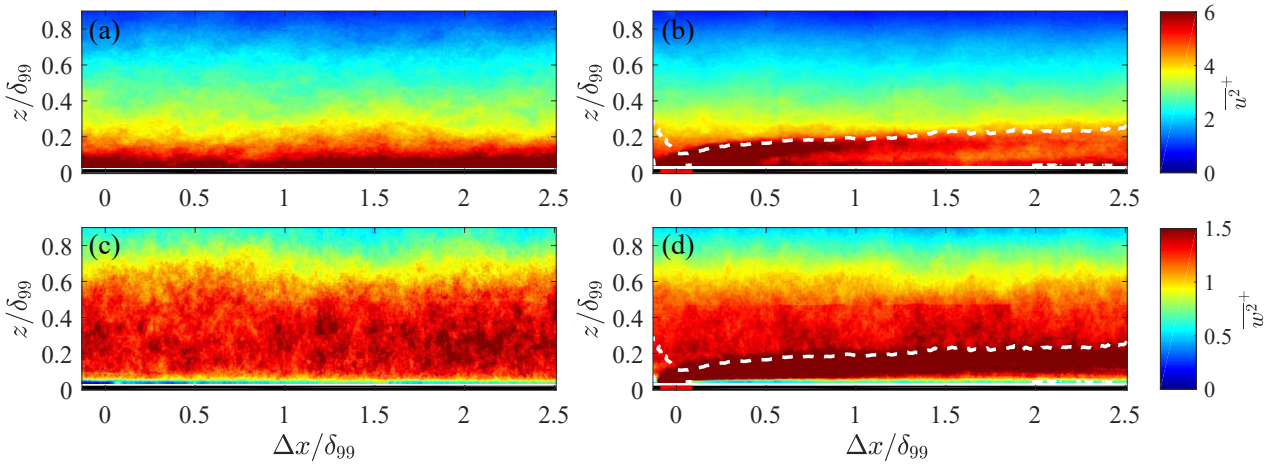

Figure 6: (a,c) show colour contours of streamwise and wall-normal turbulence intensity, $\overline{u^2}^+$ and $\overline{w^2}^+$, for the uncontrolled (canonical) turbulent boundary layer. Similarly, (b,d) correspond to $\overline{u^2}^+$ and $\overline{w^2}^+$ from the opposing controlled turbulent boundary layer. All quantities are non-dimensionlised by u_τ^2, where u_τ is the mean skin-friction velocity for both cases. The white dashed lines is the jet trajectory contour adapted from figure 5(b, d).

which compares the streamwise and wall-normal turbulence intensity ($\overline{u^2}^+$ and $\overline{w^2}^+$) for the canonical and opposing control scheme turbulent boundary layers. As expected, the canonical boundary layer, in figure 6(a,c), exhibits a high degree of streamwise homogeneity (with the remaining inhomogeneity largely a measure of the lack of convergence from the limited number of snapshots). In contrast, figure 6(d) exhibits a significant increase in $\overline{w^2}^+$ within the jet trajectory (highlighted by the white-dashed contour), which extends beyond the streamwise extent of the FOV. This jet trajectory is adapted from the figure 5(b) showing the region with $\Delta U/U_\infty < -0.005$. The streamwise intensity, $\overline{u^2}^+$, is mostly energised at $\Delta x < \delta$ in 6(b) and appears to attenuate further downstream. This is likely due to jets actively targeting high-speed structures in the opposing control scheme, which in turn leads to a decrease in the amplitude of $\overline{u^2}^+$ further downstream. These observations are also in agreement with Abbassi et al. (2017) via the use of an identical opposing control configuration.

3.4 Phase-averaged flow-fields

The mean-statistics shown so far include all images captured, which masks the instantaneous details of the interaction between the jet flow and the targeted high momentum LSMs. In order to explore this interaction conditional/phase-averaged flow fields are computed based on laser delay τ_h (introduced in figure 4). Specifically, only images captured during a high-velocity event are included and binned based on the τ_h with a bandwidth of 12.5ms to generate phase averaged flow-fields. The results are presented in figure 7, which presents colour contours of the ensemble averaged streamwise and spanwise velocity fluctuations, $\langle u \rangle$ and $\langle w \rangle$, in the right and left columns, respectively. On the bottom of each diagram, a red bar represents the conditional phase (τ_h) as a streamwise distance of the jet-flow by invoking Taylor's frozen hypothesis.

The results reveal that as the phase delay increases, the jet flow interacts with the targeted high-speed large-scale feature in the logarithmic region. Qualitatively, it is evident that the jet flow imposes an inclined 'barrier' that deflects the high-velocity fluctuations away from the wall. However, at larger τ_h it is evident that the modified structure overpowers the perturbation from the jets and shows a stronger large-scale streamwise turbulence energy.

4 Conclusions

This study presents a set of Particle Image Velocimetry (PIV) experiments to examine a high Reynolds number turbulent boundary layer that has been actively perturbed by a spanwise array of cross-flow jets. Specifically, an opposing control scheme is employed, which senses the passage of large scale high speed

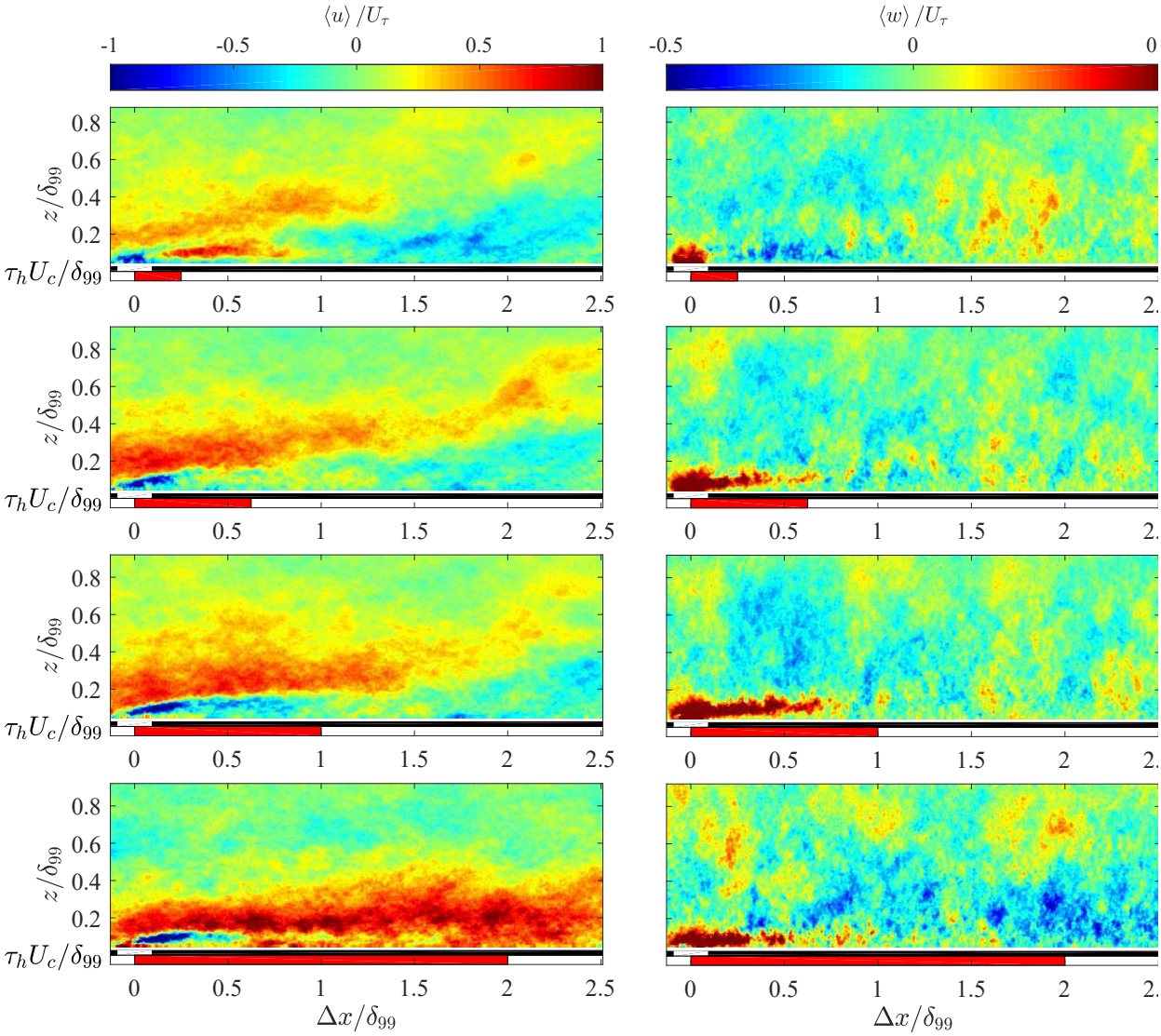

Figure 7: Colour contours of the ensemble averaged mean steamwise (left columns) and wall-normal (right columns) velocity fields, $\langle U \rangle$ and $\langle W \rangle$, conditioned on the delay of the laser pulse to the nearest jet-actuation, τ_h. The red bar under each contour plot is representative of delay τ_h and is analogous to the streamwise spatial extent the jet is on.

events using an upstream array of sensors, and actuates a spanwise array of wall-normal jets, to perturb the detected events. This control scheme is synchronised with a PIV system that captures a uniquely large field-of-view using multiple consumer-cameras that acquire DE-PIV images.

Preliminary findings from the experiments reveal that the mean streamwise velocity is modified across the captured FOV, extending beyond 2.5δ. Further, we observe that the streamwise turbulence intensity appears attenuated up to wall normal height of $z^+ \approx 2000$ after 1δ downstream of the jet actuation, while the wall-normal turbulence intensity is energised throughout the captured FOV. The underlying modified turbulent structures for the opposing control scheme are revealed by computing phase-averaged flow-fields, where the low-momentum jet-flow is observed to deflect the high-velocity large-scale structures away from the wall. To better understand the role of LSMs in a high Reynolds number boundary layers, control strategies firing at different portions of the LSMs will be examined in a future study. Moreover, the influence of these LSMs on the turbulent skin-friction will be examined by analyzing the fluctuating wall shear stress measured by the hot-film sensors from the downstream measurement array.

References

Abbassi MR, Baars WJ, Hutchins N, and Marusic I (2017) Skin-friction drag reduction in a high-Reynolds-number turbulent boundary layer via real-time control of large-scale structures. *Int J Heat Fluid Flow* 67:30–41

Baidya R, Philip J, Hutchins N, Monty J, and Marusic I (2017) Distance-from-the-wall scaling of turbulent motions in wall-bounded flows. *Physics of Fluids* 29:020712

de Silva C, Chauhan K, Atkinson C, Buchmann N, Hutchins N, Soria J, and Marusic I (2012) Implementation of large scale piv measurements for wall bounded turbulence at high reynolds numbers. in *Proceedings of 18th Australasian Fluid Mechanics Conference*. pages 3–7

de Silva CM, Gnanamanickam EP, Atkinson C, Buchmann NA, Hutchins N, Soria J, and Marusic I (2014) High spatial range velocity measurements in a high Reynolds number turbulent boundary layer. *Physics Fluids* 26:025117

de Silva CM, Grayson K, Scharnowski S, Kähler CJ, Hutchins N, and Marusic I (2018) Towards fully-resolved PIV measurements in high reynolds number turbulent boundary layers with DSLR cameras. *J Vis* 21:369–379

Hutchins N and Marusic I (2007) Large-scale influences in near-wall turbulence. *Phil Trans R Soc A,* 365:647–664

Hutchins N, Monty JP, Ganapathisubramani B, Ng HCH, and Marusic I (2011) Three-dimensional conditional structure of a high-Reynolds-number turbulent boundary layer. *J Fluid Mech* 673:255–285

Lee J, Monty J, Hutchins N et al. (2016) Validating under-resolved turbulence intensities for piv experiments in canonical wall-bounded turbulence. *Experiments in Fluids* 57:129

Lenaers P, Li Q, Brethouwer G, Schlatter P, and Örlü R (2012) Rare backflow and extreme wall-normal velocity fluctuations in near-wall turbulence. *Physics of fluids* 24:035110

Marusic I, Monty JP, Hultmark M, and Smits AJ (2013) On the logarithmic region in wall turbulence. *J Fluid Mech* 716

Mathis R, Hutchins N, and Marusic I (2009) Large-scale amplitude modulation of the small-scale structures in turbulent boundary layers. *J Fluid Mech* 628:311–337

Scarano F (2001) Iterative image deformation methods in PIV. *Meas Sci Tech* 13:R1–19

Willert C (1997) Stereoscopic digital particle image velocimetry for application in wind tunnel flows. *Meas Sci Tech* 8:1465